



IEEE TRANSACTIONS ON

GEOSCIENCE AND REMOTE SENSING

A PUBLICATION OF THE IEEE GEOSCIENCE AND REMOTE SENSING SOCIETY

JANUARY 2000

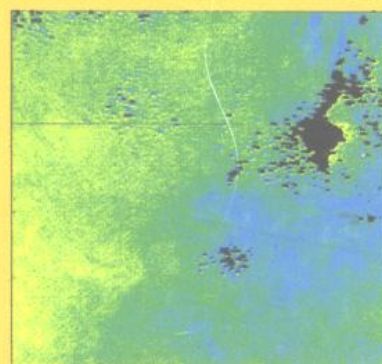
VOLUME 38

NUMBER 1

IGRSD2

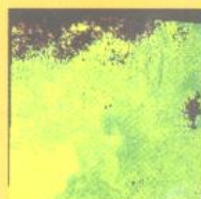
(ISSN 0196-2892)

PART I OF TWO PARTS



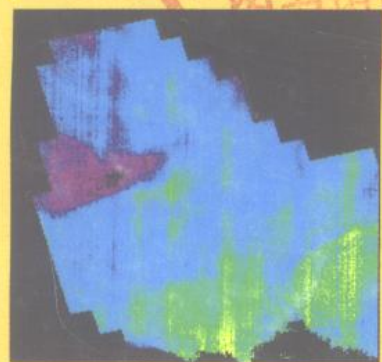
Atlantic Ocean (Jan. 29, 1998)

SeaWiFS



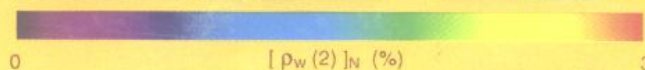
Mediterranean Sea (Feb. 28, 1998)

SeaWiFS



Adriatic Sea (Sep. 24, 1997)

SeaWiFS



Retrieved ocean-normalized, water-leaving reflectance (443 nm) from MOS compared with SeaWiFS.



IEEE TRANSACTIONS ON

GEOSCIENCE AND REMOTE SENSING

A PUBLICATION OF THE IEEE GEOSCIENCE AND REMOTE SENSING SOCIETY

JANUARY 2000

VOLUME 38

NUMBER 1

IGRSD2

(ISSN 0196-2892)

PART I OF TWO PARTS

REGULAR PAPERS

Subsurface Sensing

- Dispersion Analysis of Crack-Waves in an Artificial Subsurface Fracture Using Two Crack Models *K. Nagano and H. Niitsuma* 3
- Area-Based Results for Mine Detection *E. Gelenbe and T. Koçak* 12
- Nonlinear Inversion in Electrode Logging in a Highly Deviated Formation with Invasion Using an Oblique Coordinate System *A. Abubakar and P. M. van den Berg* 25
- Quantitative Performance Evaluation of the Lossless Compression Approach Using Pole-Zero Modeling *Y. W. Nijim, S. D. Stearns, and W. B. Mikhael* 39

Microwave Remote Sensing

- Detection of Calibration Drifts in Spaceborne Microwave Radiometers Using a Vicarious Cold Reference *C. S. Ruf* 44
- Metamorphic Signature of Snow Revealed in SSM/I Measurements *S. Rosenfeld and N. C. Grody* 53
- The Normalized Radar Cross Section of the Sea at 10° Incidence *V. Hesany, W. J. Plant, and W. C. Keller* 64
- Dual-Polarized Ku-Band Backscatter Signatures of Hurricane Ocean Winds *S. H. Yueh, R. West, F. K. Li, W.-Y. Tsai, and R. Lay* 73
- Improved Resolution Backscatter Measurements with the SeaWinds Pencil-Beam Scatterometer *M. W. Spencer, C. Wu, and D. G. Long* 89
- Sensitivity to Soil Moisture By Active and Passive Microwave Sensors *Y. Du, F. T. Ulaby, and M. C. Dobson* 105

Radar Remote Sensing

- Simulation of Interferometric SAR Response for Characterizing the Scattering Phase Center Statistics of Forest Canopies *K. Sarabandi and Y.-C. Lin* 115
- Determining Land-Surface Parameters from the ERS Wind Scatterometer *I. H. Woodhouse and D. H. Hoekman* 126

Optical Remote Sensing

- Raman Lidar Calibration for the DMSP SSM/T-2 Microwave Water Vapor Sensor *J. Wessel, S. M. Beck, Y. C. Chan, R. W. Farley, and J. A. Gelbwachs* 141
- Infrared Tomographic System for Monitoring the Two-Dimensional Distribution of Atmospheric Pollution over Limited Areas *F. Cuccoli, L. Facheris, S. Tanelli, and D. Giuli* 155
- Practical Methods for Rapid and Accurate Computation of Interferometric Spectra for Remote Sensing Applications ... *C. D. Barnett, J. M. Blaisdell, and J. Susskind* 169
- Comparing the Ocean Color Measurements Between MOS and SeaWiFS: A Vicarious Intercalibration Approach for MOS *M. Wang and B. A. Franz* 184

(Continued on p. 2)

(Continued from p. 1)

Modulations of Laser Signals by Water Waves Observed by a Boxcar Integrator	C. S. Lin	198
---	-----------	-----

Atmospheric Remote Sensing

Precipitation Detection by the TOPEX/Poseidon Dual Frequency Radar Altimeter, TOPEX Microwave Radiometer, Special Sensor Microwave/Imager and Climatological Shipboard Reports	D. Cailliau and V. Zlotnicki	205
Improvements and Complications Involved with Adding an 85-GHz Channel to Cloud Liquid Water Radiometers	J. P. Bobak and C. S. Ruf	214
A Nonlinear Multispectral Statistical CLEAN-Based Precipitation Parameter-Retrieval Algorithm	G. M. Skofronick-Jackson and A. J. Gasiewski	226

Electromagnetic Problems and Computations

A Coherent Scattering Model to Determine Forest Backscattering in the VHF-Band	H. Israelsson, L. M. H. Ulander, T. Martin, and J. I. H. Askne	238
A Note on the Multiple Scattering in an IEM Model	K. S. Chen, T.-D. Wu, M.-K. Tsay, and A. K. Fung	249

Signal and Image Processing

A Fuzzy-Possibilistic Scheme of Study for Objects with Indeterminate Boundaries: Application to French Polynesian Reefscapes	S. Andréfouët, L. Roux, Y. Chancerelle, and A. Bonneville	257
Nonparametric Estimation of Mean Doppler and Spectral Width	J. M. B. Dias and J. M. N. Leitão	271
The Relationship Between the Matched-Filter Operator and the Target Signature Space-Orthogonal Projection Classifier	S. Johnson	283
An Explicit Fuzzy Supervised Classification Method for Multispectral Remote Sensing Images	F. Melgani, B. A. R. Al Hashemy, and S. M. R. Taha	287
An Imaging Algorithm of Objects Embedded in a Lossy-Dispersive Medium for Subsurface Radar-Data Processing ...	T. Sato, T. Wakayama, and K. Takemura	296

COMMUNICATIONS

Multispectral Image Feature Selection for Land Mine Detection	G. A. Clark, S. K. Sengupta, W. D. Aimonetti, F. Roeske, and J. G. Donetti	304
Estimation of Soil-Type Heterogeneity Effects in the Retrieval of Soil Moisture from Radiobrightness	J. F. Galantowicz, D. Entekhabi, and E. G. Njoku	312
Potential and Limitations of RADARSAT SAR Data for Wet Snow Monitoring	N. Baghadi, Y. Gauthier, M. Bernier, and J.-P. Fortin	316
The "Myth" of the Minimum SAR Antenna Area Constraint	A. Freeman, W. T. K. Johnson, B. Huneycutt, R. Jordan, S. Hensley, P. Siqueira, and J. Curlander	320
The Systematic Behavior of Water Vapor estimates Using Four Years of GPS Observations	T. R. Emardson, J. Johansson, and G. Elgered	324
On the Condition Number of Gaussian Sample-Covariance Matrices	A. B. Kostinski and A. C. Koivunen	329

ANNOUNCEMENTS

Call for Papers—TGARS Special Issue on Analysis of Hyperspectral Image Data		333
Call for Papers—TGARS Special Issue on New Advances in Subsurface Sensing: Systems, Modeling, and Signal Processing		334
IEEE Copyright Form		335

About the Cover: The cover image shows the retrieved ocean normalized water-leaving reflectance (443 nm) from the German Modular Optoelectronic Scanner (MOS) compared with NASA's Sea-Viewing Wide Field-of-View Sensor (SeaWiFS) for a co-located scene acquired on (a) January 29, 1998 in the Atlantic Ocean, (b) February 28, 1998 in the Mediterranean Sea, and (c) September 24, 1997 in the Adriatic Sea. In deriving these results, a consistent atmospheric correction algorithm was applied to both sensors, and a vicarious intercalibration method was used for MOS. For more information, see the paper by M. Wang and B. A. Franz "Comparing the ocean color measurements between MOS," which begins on p. 184.

Dispersion Analysis of Crack-Waves in an Artificial Subsurface Fracture Using Two Crack Models

Koji Nagano and Hiroaki Niitsuma

Abstract—We investigated crack-wave dispersions in an artificial subsurface fracture both experimentally and numerically using a wavelet analysis and two crack models. Crack-waves are seismic modes that propagate along a fracture. The dispersion characteristics of crack-waves depend on the geometry and physical properties of a fracture. We measured crack-waves at an artificial subsurface fracture in Higashi-Hachimantai Hot Dry Rock model field, Japan. This subsurface fracture is at a depth of about 370 m. During a measurement, we injected water into the fracture and changed the interface conditions of the fracture. A wavelet analysis provided the dispersion of the arrival times of crack-waves. The crack-waves showed positive velocity dispersion; i.e., low frequency components arrived later. As wellhead pressure increased due to water injection, the dispersion characteristics changed. A low-velocity-layer (LVL) model and a crack-stiffness model were examined to explain crack-wave dispersion. In the LVL model, rock layers with a low velocity surround a fluid layer. There is no contact between the LVL's. On the other hand, the crack-stiffness model considers crack stiffness due to contact between asperities on fracture surfaces. The arrival-time curves calculated by the crack-stiffness model showed a good fit to the measured values. As wellhead pressure increased, crack stiffness decreased and thickness of a fluid layer increased. In contrast, the LVL model did not adequately duplicate the measured data.

Index Terms—Crack, crack-waves, dispersion, wavelet.

I. INTRODUCTION

A FLUID-FILLED crack and a fracture zone with low velocities act as elastic interfaces for seismic waves. Such interfaces trap seismic waves, and trapped seismic waves propagate along the interfaces. They are referred to as crack-waves, crack-interface waves, and fault zone-guided waves [1]–[3]. In this paper, we refer to these seismic modes as crack-waves. The propagation characteristics of crack-waves are different from those of reflected or refracted seismic waves, which are used in conventional seismic surveys. Their waveforms (e.g., velocity-frequency dispersion and amplitude-space distribution) are strongly dependent on the crack's geometry and its physical properties. Therefore, measurement of crack-waves is an effective tool for characterizing a subsurface fracture.

Manuscript received July 1, 1998; revised March 24, 1999. This work was supported by a Grant-in Aid for Encouragement of Young Scientists, Ministry of Education, Science, and Culture of Japan under Contracts 08751081 and 10750667 and the Espec Foundation for Earth Environmental Research and Technologies (Charitable Trust), and was conducted as part of the MTC (More Than Cloud) international collaborative project funded by NEDO, Japan.

K. Nagano is with the Department of Computer Science and Systems Engineering, Muroran Institute of Technology, Muroran 050-8585, Japan (e-mail: nagano@csse.muroran-it.ac.jp).

H. Niitsuma is with the Department of Geoscience and Technology, Graduate School of Engineering, Tohoku University, Sendai 980-8579, Japan (e-mail: niitsuma@ni4.earth.tohoku.ac.jp).

Publisher Item Identifier S 0196-2892(00)00001-2.

We previously studied the propagation of crack-waves to characterize subsurface fractures [4]–[7]. We detected crack-waves propagating along an artificial subsurface fracture, which was saturated with water at a depth of 370 m in Higashi-Hachimantai Hot Dry Rock model field, Japan [4]. We estimated the dimensionless crack stiffness of the fracture surfaces based on dispersions of the crack-waves [5], [8]. In this analysis, we applied a pseudo-Wigner-Ville distribution (PWD) to estimate the dispersions of crack-waves. However, it was difficult to estimate dispersions because of cross terms in the PWD. Cross terms naturally occur in energy densities of the PWD. The dimensionless crack stiffness is calculated from three physical properties of a fracture (thickness of the fluid layer, crack stiffness, and the shear modulus of the solid). We could not estimate the primary physical properties of a fracture in the crack-wave analysis, because the dimensionless crack stiffness is a theoretical parameter.

Niitsuma and Saito [9] and Tanaka *et al.* [10] reported that a low-velocity zone could be found close to an artificial subsurface fracture that had been created in an intact rock layer by hydraulic fracturing. The velocity of a compressional wave decreased in a path through the fracture when wellhead pressure increased due to water injection into the fracture. There was no natural crack in the rock layer before hydraulic fracturing. They explained this decrease in compressional wave velocity in terms of the reopening of microcracks in the vicinity of the fracture. This phenomenon indicates that a low-velocity zone is essential for subsurface fractures. Therefore, it is important to estimate the low-velocity zone when subsurface fractures are analyzed.

The numerical analysis of crack-waves trapped in a single fluid-filled crack has been reported by Chouet [1], Ferrazzini and Aki [11], and Hayashi and Sato [8]. All of these authors addressed very slow waves with positive dispersion. Chouet, and Ferrazzini and Aki used a simple three-layer model for a subsurface crack. A very thin fluid layer, compared with the wavelength, was sandwiched between two solid half-spaces. Hayashi and Sato focused on the contact between asperities on fracture surfaces [8]. The dimensionless crack stiffness was used to represent contact in their crack model.

In this study, we investigate the opening of a subsurface fracture by comparing the dispersions of crack-waves measured in the field and numerical results calculated using two crack models. The crack-waves were measured at an artificial subsurface fracture at a depth of about 370 m. Two waveforms of the crack-waves, which were recorded at the beginning of water injection and at the maximum wellhead pressure during water injection, are analyzed. The wavelet transform (WT) provides a time-frequency representation of the arrival time of

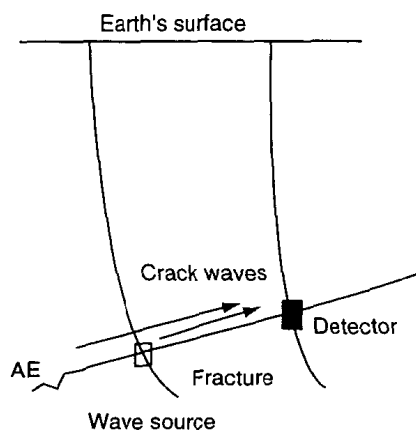


Fig. 1. Concept of crack-wave measurement.

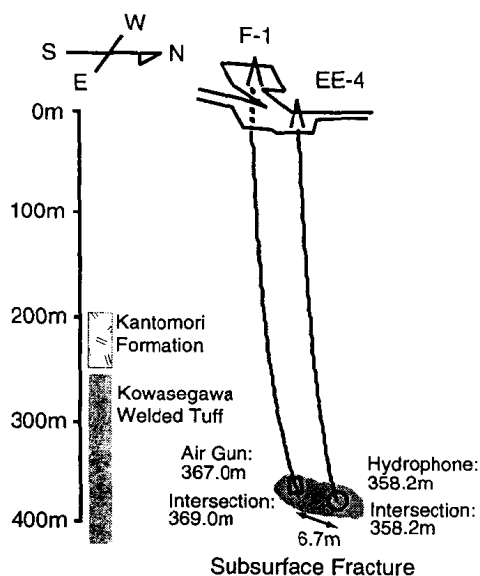


Fig. 2. Higashi-Hachimantai HDR model field. Wells EE-4 and F-1 intersect an artificial subsurface fracture at depths of 358.2 and 369.0 m, respectively.

crack-waves. The two crack models are the crack-stiffness model, which was investigated by Hayashi and Sato [8], and the low-velocity layer (LVL) model, which is a modified three-layer model based on the experimental results of Niitsuma and Saito [9]. We calculate the arrival time curves of crack-waves with the two crack models and fit these curves to the spectral data in the time-frequency representation from the WT. We estimate the physical parameters of the crack models in the opening of a fracture based on crack-wave dispersions.

II. CRACK-WAVE MEASUREMENT IN HIGASHI-HACHIMANTAI HOT DRY ROCK (HDR) MODEL FIELD

Crack-waves were measured at Higashi-Hachimantai Hot Dry Rock (HDR) model field, Japan [12]. Fig. 1 illustrates the concept of a crack-wave measurement. Crack-waves can be detected at the intersection of a bore hole and the fracture. Fig. 2 depicts Higashi-Hachimantai HDR model field. An artificial subsurface fracture was created in intact, welded tuff at a depth of 369.0 m in well F-1 by hydraulic fracturing. During hydraulic fracturing, 40-mesh sand was injected as a propping agent. Core samples of well F-1 showed no significant joint or crack before the fracturing. Well EE-4 was drilled

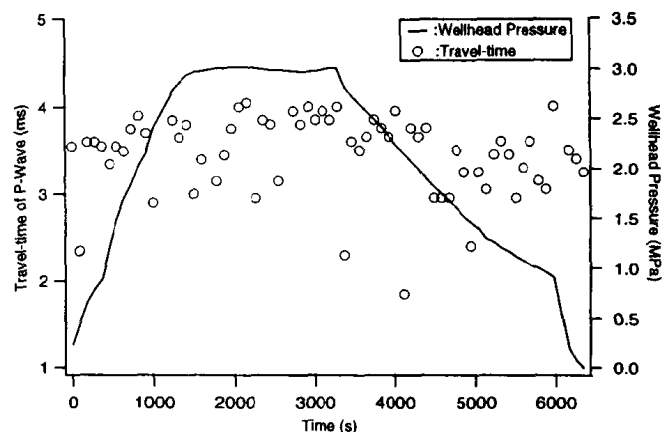


Fig. 3. Wellhead pressure and travel time of the compressional wave during water injection.

into the artificial fracture after the hydraulic fracturing and intersected the artificial fracture at a depth of 358.2 m. The distance between the intersection points of wells F-1 and EE-4 was 6.7 m. The radius of the fracture was about 60 m [12]. A transmissibility test showed that the fracture aperture was about 0.08 mm without pressurization and 0.2 mm at a wellhead pressure of 3.0 MPa [13]. The transmissibility test also showed that the reopening pressure of this fracture system was about 2.8 MPa at the wellhead. The velocities of compressional and shear waves of intact rock in this field are 3100 m/s and 1860 m/s, respectively [10].

We carried out our measurements using this single artificial fracture. A downhole air gun was used as a wave source at a depth of 367.0 m in well F-1. The air gun was suspended two meters from the intersection of the fracture so that we would not damage the bore hole at the intersection. A hydrophone was suspended at a depth of 358.2 m in well EE-4 (i.e., at the intersection with the fracture), to measure the crack-waves. This hydrophone has a flat sensitivity in a frequency range of 60 Hz to 10 kHz, and its sensitivity gradually decreases for frequency components below 60 Hz.

We pressurized the subsurface fracture to vary the interface conditions of the fracture. The wellheads of both wells were closed with wireline lubricators. Wellhead pressure was measured in well F-1. Since circulation loss and friction loss in the bore holes and this fracture system are small, the wellhead pressure in well EE-4 is almost equal to that in well F-1 [12]. Fig. 3 shows the wellhead pressure during crack-wave measurement. After we held the wellhead pressure at 3.0 MPa for 30 min, we closed the wellheads completely. Wellhead pressure subsequently decreased naturally due to permeation into the rock.

Fig. 3 also shows the travel time of a compressional wave in the crack-wave measurement. Since the air gun was two meters above the intersection of the bore hole and the hydrophone was at another intersection, the path of the compressional wave was close to the fracture. The velocity of the compressional wave was calculated from the travel time and the distance, 6.7 m, between the intersections of the bore holes and the fracture. The velocity was 1900 m/s at the beginning of water injection and 1700 m/s when the wellhead pressure was constant at 3.0 MPa for about 30 min. These velocities are lower than that measured in other experiments in this field [10]. Another water-injection

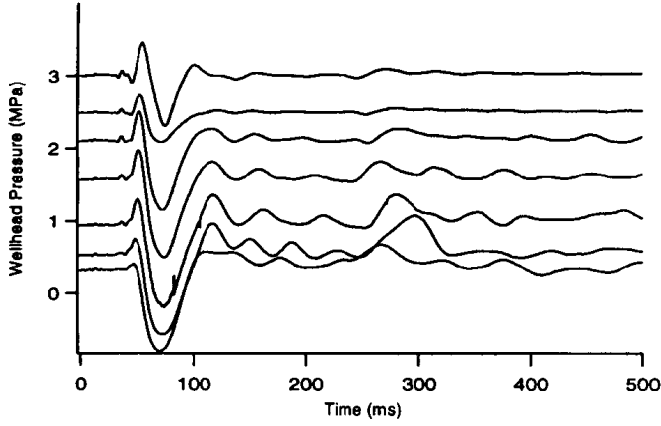


Fig. 4. Crack-waves during water injection in an artificial subsurface fracture. The crack-waves arrive at 40 ms.

test was carried out about one hour before the crack-wave measurement. These lower velocities indicate that the rock near the fracture was undergoing relaxation after the previous water-injection.

Fig. 4 shows waveforms detected during water injection. The crack-waves convert to tube waves at the intersection with a bore hole. Tube-wave analysis indicated that the waves with a large amplitude at 40 ms in Fig. 4 are crack-waves [4]. As the wellhead pressure was increased, the waveforms of the crack-waves changed.

III. WAVELET ANALYSIS OF CRACK-WAVES

We used the wavelet transform (WT) to obtain spectral data as a function of arrival time in a dispersion analysis of the crack-waves [14]–[16]. Time and frequency resolutions vary in the WT, while they are uniform in the traditional short-time Fourier transform (STFT). This variable resolution is an advantage of the WT over the STFT. The WT is defined as

$$W_\phi(a, b) = \frac{1}{\sqrt{a}} \int_{-\infty}^{\infty} \phi^* \left(\frac{t' - b}{a} \right) s(t') dt' \quad (1)$$

where $\phi(t)$ is the analyzing wavelet, a is a scale parameter, b is a time-shift parameter, and $*$ denotes the complex conjugate. The scale parameter a is the reciprocal of the frequency. The analyzing wavelet requires the admissibility condition given by

$$c_\phi = 2\pi \int_{-\infty}^{\infty} \frac{|\hat{\phi}(\omega)|^2}{|\omega|} d\omega < \infty \quad (2)$$

where $\hat{\phi}$ is a Fourier transform of the analyzing wavelet ϕ . The analyzing wavelet in this paper is the modulated Gaussian $\phi_M(t)$ given by

$$\phi_M(t) = \exp \left(-\frac{t^2}{2} + jmt \right). \quad (3)$$

When the analyzing wavelet is the modulated Gaussian, uncertainty in the time-frequency domain is minimum. Therefore, the modulated Gaussian is efficient for representing a spectral component that varies with time. The modulated Gaussian does not strictly satisfy the admissibility condition. However, if $m > 5$

in (3), we can consider that the admissibility condition is satisfied [17]. In the WT calculation, we set $m = 6$.

We analyzed the WT of the crack-waves in a frequency range between 2 and 256 Hz because of the frequency components of the air gun. The waveforms and squared amplitudes of the WT are presented in Fig. 5. Fig. 5(a) shows the crack-waves detected at the beginning of water injection. The wellhead pressure is 0.4 MPa. The crack-waves in Fig. 5(b) were detected when the wellhead pressure was held constant at 3.0 MPa for about 30 min. The squared amplitude of the WT was normalized by its maximum value at each frequency to enhance the contrast of the variation in time for frequency components with small amplitude. The air gun exploded seismic waves at a frequency range below 300 Hz simultaneously [5]. Crack-waves are dispersive, since arrival time (which occurs at the onset of the relative maxima) is a function of frequency in Fig. 5. The lower frequency components of the crack-waves arrive later. The velocity dispersion at a wellhead pressure of 0.4 MPa is weaker than that at a wellhead pressure of 3.0 MPa.

IV. CRACK MODELS

A basic crack model for a fluid-filled crack is a three-layer model, as discussed by Ferrazzini and Aki [11], in which a thin fluid layer, compared with the wavelength of the crack-waves, is sandwiched between two solid half-spaces. There is no contact between the two solids. The three-layer model is not valid for the analysis of crack-waves propagating along an artificial subsurface fracture. In particular, since a low-velocity zone was detected even in the vicinity of a fracture created in an intact rock layer [9], [10], a low-velocity zone should be taken into account in an analysis of subsurface fractures. Contact between asperities on fracture surfaces is also inherent in subsurface fracture.

We examined crack-wave dispersions using two crack models: the LVL model and the crack-stiffness model. The two physical properties, a low-velocity zone and contact, are independently introduced into a three-layer model. These crack models, which are independent of each other, demonstrate the effects of these physical properties of a fracture.

Dispersion equations for the LVL and crack-stiffness models are derived using common potential functions for the wave equation. We assume that layers lie in the xy -plane and that the normal to the wavefront lies on the x axis. Periodic solutions of the wave equation may be found by combining with a compressional wave solution

$$\phi_m = (\Delta'_m e^{-j\xi r_{\alpha m} z} + \Delta''_m e^{j\xi r_{\alpha m} z}) e^{j(\omega t - \xi x)} \quad (4)$$

and a shear wave solution

$$\psi_m = (\Omega'_m e^{-j\xi r_{\beta m} z} + \Omega''_m e^{j\xi r_{\beta m} z}) e^{j(\omega t - \xi x)} \quad (5)$$

where ω is the angular frequency, ξ is the wavenumber, and Δ'_m , Δ''_m , Ω'_m , and Ω''_m are unknown functions of ω and ξ . Subscript m denotes the number of a layer.

Higher order modes show more oscillation of pressure along the z axis in a fluid layer. The aperture of a fluid layer is quite narrow in this analysis. Therefore, higher order modes have much less energy than the fundamental mode. The numerical

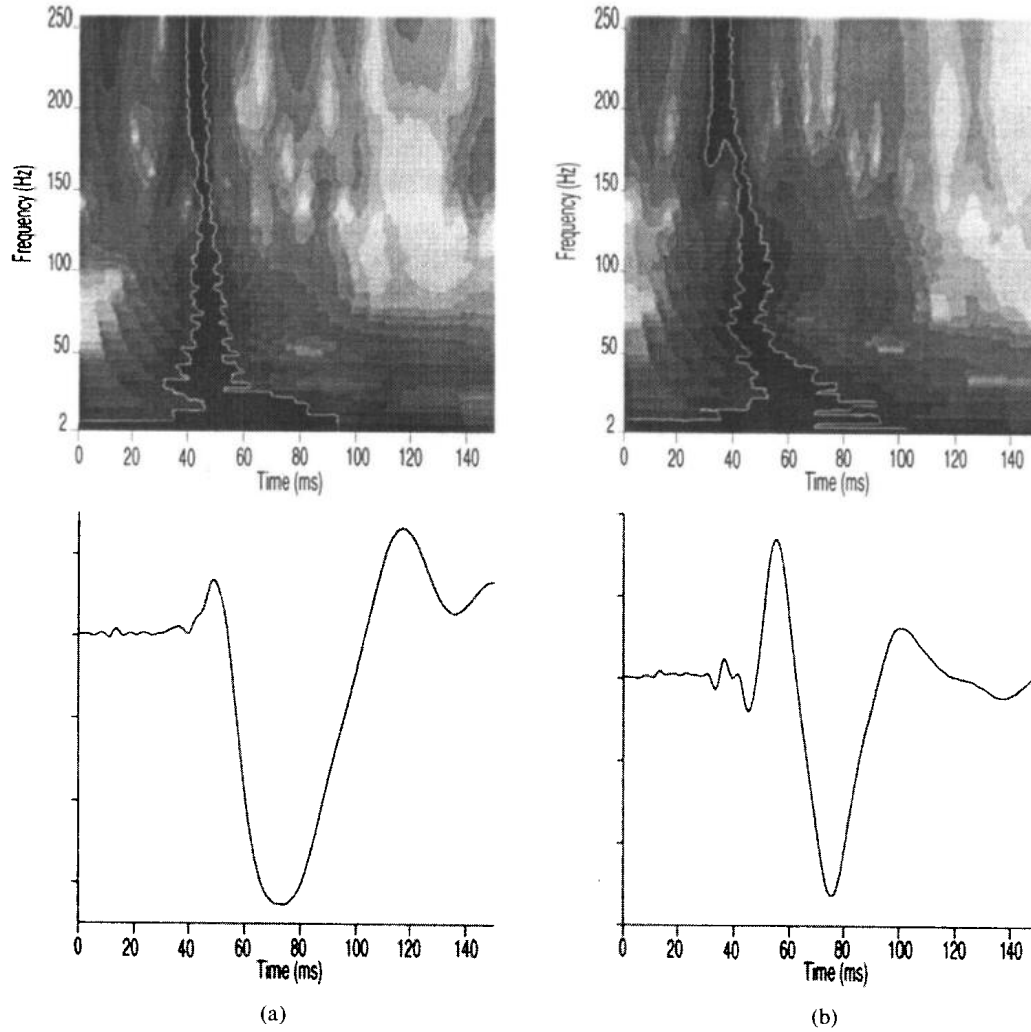


Fig. 5. Wavelet transforms of the crack-waves. The arrival time of each frequency component can be seen. (a) The crack-wave detected at a wellhead pressure of 0.4 MPa. These data were recorded at the beginning of the injection. (b) The crack-wave detected when the wellhead pressure was held constant at 3.0 MPa for 1779 s (about 30 min). The aperture of the subsurface fracture increases when the wellhead pressure approaches 3.0 MPa.

analysis of Ferrazzini and Aki [11] showed that only the fundamental symmetric mode of crack-waves was strongly affected by the interface conditions at fracture surfaces. Therefore, in this paper, we analyzed the fundamental symmetric modes. Since the velocities of fundamental symmetric modes of crack-waves are lower than the fluid velocity, in the above potential functions

$$\begin{aligned} r_{\alpha m} &= -j \sqrt{1 - \left(\frac{v}{\alpha_m}\right)^2}, \\ r_{\beta m} &= -j \sqrt{1 - \left(\frac{v}{\beta_m}\right)^2} \end{aligned} \quad (6)$$

where v is the phase velocity of crack-waves, and α_m and β_m are the velocities of compressional and shear waves of the m th layer.

A. Low-Velocity Layer (LVL) Model

Fig. 6 schematically presents the LVL model. Additional solid layers are found on both sides of the fluid layer. The velocities of these two solid layers are lower than those of the top and bottom bedrock layers. The low-velocity layer (LVL) represents a micro crack zone that is created by pressurization caused by water injection. We assume coordinates to use the

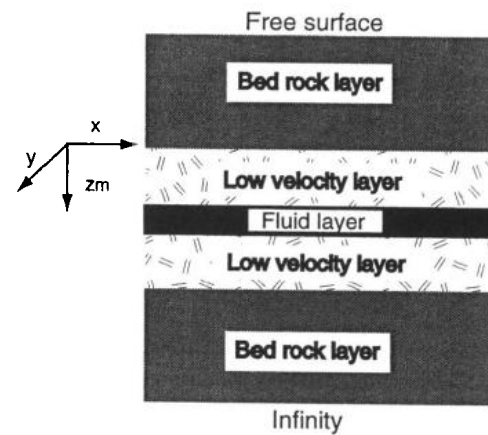
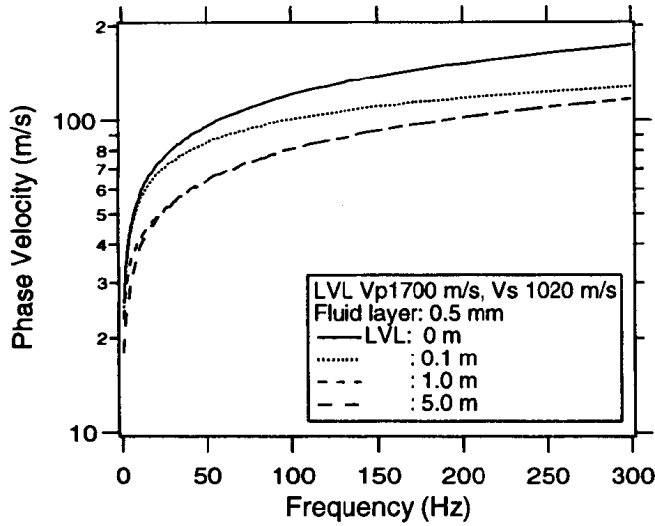
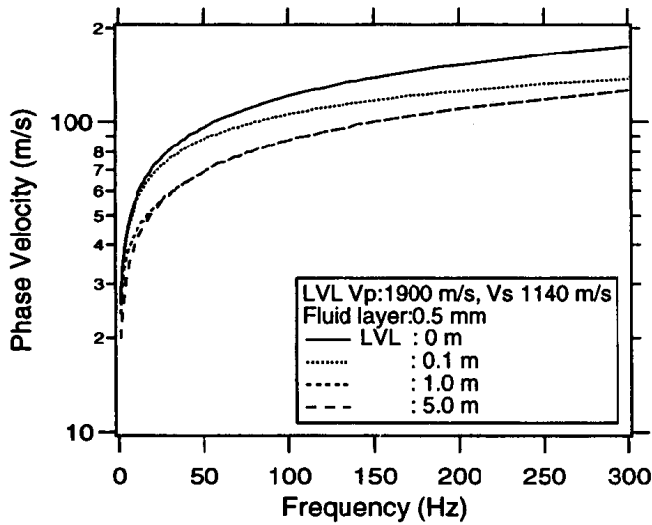


Fig. 6. Low-velocity layer model for an artificial subsurface fracture.

matrix method by Haskell [18]. The top solid layer has a free surface on one side and the bottom solid layer is an infinite half-space. The x axis is parallel to the layers in the direction of propagation. The origin of the z axis is the top surface of each layer. The z axis is positive in the direction of the medium. The layers are numbered starting from the top solid layer. The thickness of the m th layer is d_m , and the boundaries of the m th layer are at $z_m = 0$ and d_m . The m th layer is characterized by



(a)



(b)

Fig. 7. Effects of the thickness of the low-velocity layer on the phase velocity of crack-waves: (a) the compressional wave velocity in the low-velocity layer is 1700 m/s and (b) the compressional wave velocity in the low-velocity layer is 1900 m/s.

the compressional wave velocity α_m , the shear wave velocity β_m , and the density ρ_m . All of the layers are homogeneous and isotropic, and the fluid is inviscid and incompressible.

At the interface between a bedrock layer and an LVL, normal and shear stresses are continuous, as are displacements in the x and z axes.

At the interface between a fluid layer and an LVL, the normal stress and normal displacement must be continuous and shear stress vanishes. Thus

$$\left. \begin{aligned} \tau_{zz} &= -\sigma \\ w &= w_f \\ \tau_{zx} &= 0 \end{aligned} \right\} \text{ at } \begin{aligned} z_3 &= 0 \\ z_3 &= d_3 \end{aligned} \quad (7)$$

where τ_{zz} and τ_{zx} are the normal and shear stresses, respectively, σ is the pressure of the fluid, w is the displacement of the solid in the z axis, and w_f is the displacement of the fluid. Since the top surface in the first layer is free, both normal and shear stresses vanish at the top surface. There are no sources at infinity in the bottom layer, so that $\Delta_5'' = \Omega_5'' = 0$. We obtain

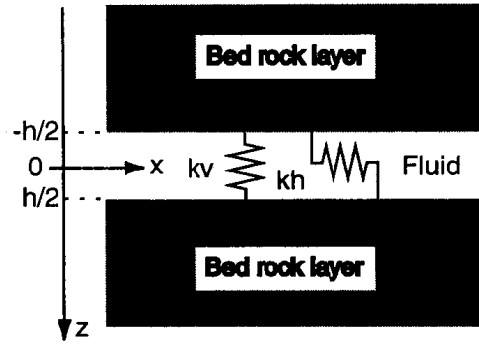


Fig. 8. Crack-stiffness model for an artificial subsurface fracture.

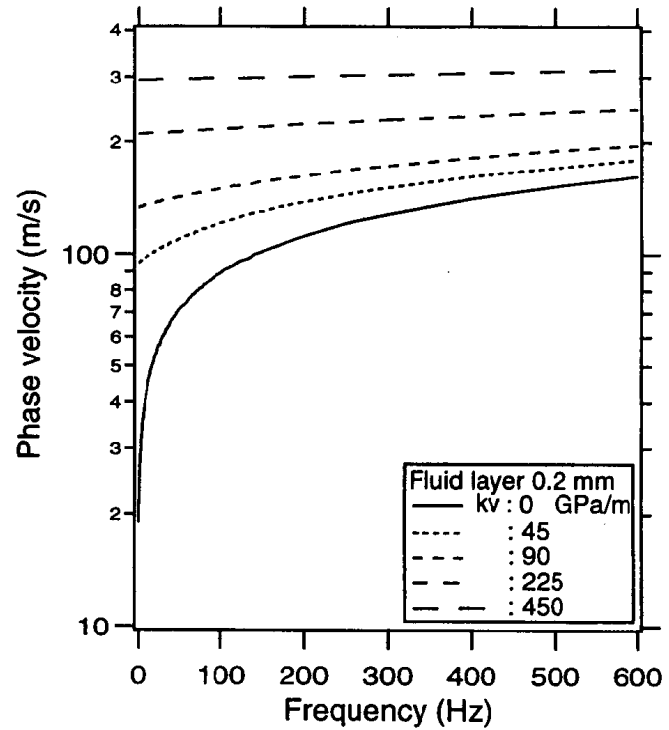


Fig. 9. Dispersion curves of crack-waves in the crack-stiffness model.

the dispersion equation that satisfies these boundary conditions using the matrix method [7], [18].

Fig. 7 shows dispersion curves in the LVL model. When the thickness of an LVL increases, velocities decrease. When the thickness of an LVL exceeds a certain limit, velocities are almost similar in a high frequency range. The limit frequency depends on the thickness of the LVL and the wavelength. For example, in Fig. 7(a), there is little difference between the dispersion curves for the LVL thicknesses of 1.0 and 5.0 m at a frequency above 30 Hz. It is difficult to measure crack-waves at a very low frequency because of the limited frequency performance of the wave source. Therefore, this convergence means that there is an upper limit for estimating the thickness of an LVL when we measure the velocities of crack-waves.

B. Crack-Stiffness Model

Fig. 8 shows the crack-stiffness model, in which contact between asperities on fracture surfaces is taken into account [8]. Two solids are connected with springs. A fluid layer is between the solids, and its thickness is h . The origin of the z axis is at

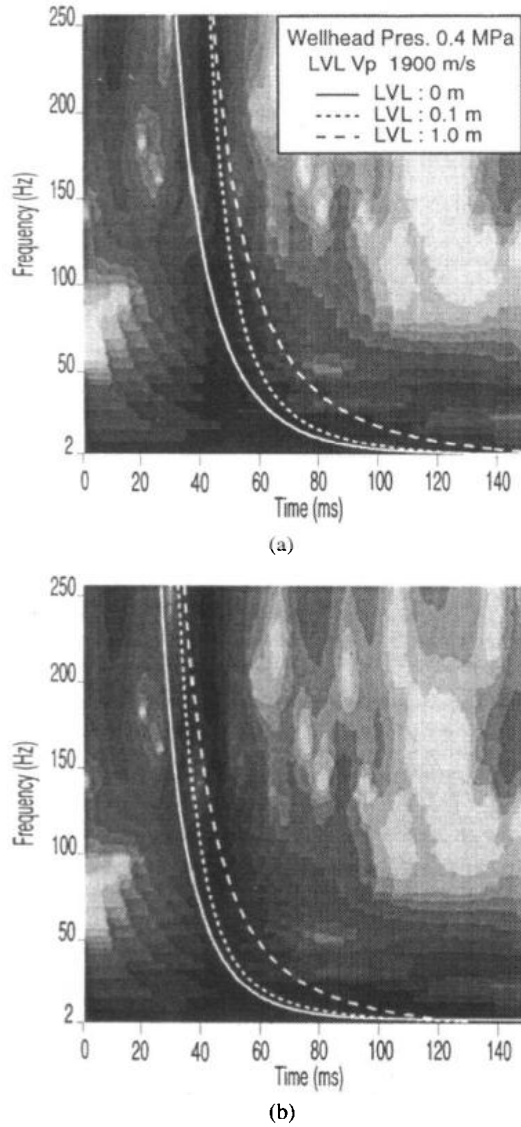


Fig. 10. Arrival times calculated from group velocities with the LVL model and a time-frequency representation of crack-waves at the beginning of water injection. (a) The fluid layer is 0.5 mm thick. (b) The fluid layer is 1.0 mm thick. Compressional and shear wave velocities are 1900 and 1140 m/s, respectively. The LVL is 0, 0.1, and 1.0 m thick in (a) and (b).

the center of the fluid layer. The boundary conditions at the interface between a fluid layer and a solid layer are

$$\left. \begin{aligned} \tau_{zx} &= k_h (u_{z=h/2} - u_{z=-h/2}) \\ \tau_{zz} &= -\sigma + k_v (w_{z=h/2} - w_{z=-h/2}) \\ w &= w_f \end{aligned} \right\} \text{ at } z = \pm \frac{h}{2} \quad (8)$$

where k_h and k_v are the specific crack stiffnesses in directions parallel and normal to the fluid layer, respectively. The symmetric mode is a function of k_h , and the antisymmetric mode is a function of k_v . A dispersion equation is obtained by substituting stresses and displacements derived from (4) and (5) into these boundary conditions [8].

Fig. 9 shows dispersion curves of crack-waves in the crack-stiffness model. The thickness of the fluid layer is 0.2 mm, and $k_v = 0, 45, 90, 225, 450$ GPa/m for calculating the dispersion curves in Fig. 9. Crack stiffness increases the phase velocities of crack-waves. Furthermore, the degree of dispersion decreases if crack stiffness increases.

V. MODELING CRACK-WAVES

To estimate the physical parameters of these two crack models from the observed crack-waves, we numerically simulate the arrival times of crack-waves for the given crack models. The contours in a scalogram represent the locations of relative maxima of wave energy in the time and frequency domains. A dispersive curve of the relative maxima is observed in the initial motions of the crack-waves in Fig. 5. We fit the arrival times of crack-waves to the dispersive relative maxima in Fig. 5. The arrival times of wave energy are calculated from group velocity and propagation distance. Group velocities are calculated from the phase velocities obtained from dispersion equations in the previous section. Because the hydrophone was suspended at the depth of the intersection with the fracture and the air gun was installed two meters above another intersection with the fracture, we neglect the distance between the air gun and the intersection. The orientation of the artificial fracture, which was estimated from tectonic stress measurement [19], is almost the same as the inclination of the artificial fracture in a core sample, which was obtained from well EE-4. Thus, we assume that the artificial fracture is not curved between the intersections of the bore holes. The propagation distance of crack-waves is 6.7 m in calculations of the arrival time.

A. Arrival-Time Curves in the LVL Model

We examined the thicknesses of the fluid layer and the LVL as parameters of the LVL model when calculated arrival times were compared with the dispersion of measured crack-waves. To simplify the calculation, the thicknesses of LVL's are the same on both sides of the fluid layer. We gave typical values for the densities of rock and fluid and fluid velocity. The densities of the bedrock layer and the LVL are 2600 kg/m³, and the density of the fluid layer is 1000 kg/m³. Fluid velocity is 1500 m/s. For other parameters of the LVL model, data measured in the field are used. Velocities of compressional and shear waves in the bedrock layer are 3100 and 1860 m/s, respectively. The velocity of a compressional wave in the LVL is 1900 m/s at the beginning of water injection and 1700 m/s at the maximum wellhead pressure. We assume that Poisson's ratio for the LVL is the same as that for the bedrock layer and is constant during water injection.

We determined the thicknesses of the fluid layer and the LVL by trial and error. Fig. 10 shows some curves for the calculated arrival times of crack-waves recorded at the beginning of water injection. The background noise level, which exists before the arrival of crack-waves, can be recognized in a contour of the scalogram when we compare the contour to a waveform (Fig. 5). The arrival of a wave occurs at the onset of a relative maximum in a scalogram. The measured crack-waves are less dispersive at a frequency above 30 Hz. On the other hand, calculated arrival-time curves show strong dispersion at frequencies below 70 Hz. Therefore, calculated arrival-time curves are not similar to the dispersion of crack-waves measured at a frequency below 70 Hz. The best combination in our trials was a fluid layer of 1.0 mm and an LVL of 0.1 m. With this combination, arrival-time curves fit in the frequency range of 70–256 Hz. None of the arrival-time curves fit the entire frequency range of 2–256 Hz in our trials.

Dispersion characteristics of crack-waves recorded at a well-head pressure of 3.0 MPa were also examined by fitting to ar-

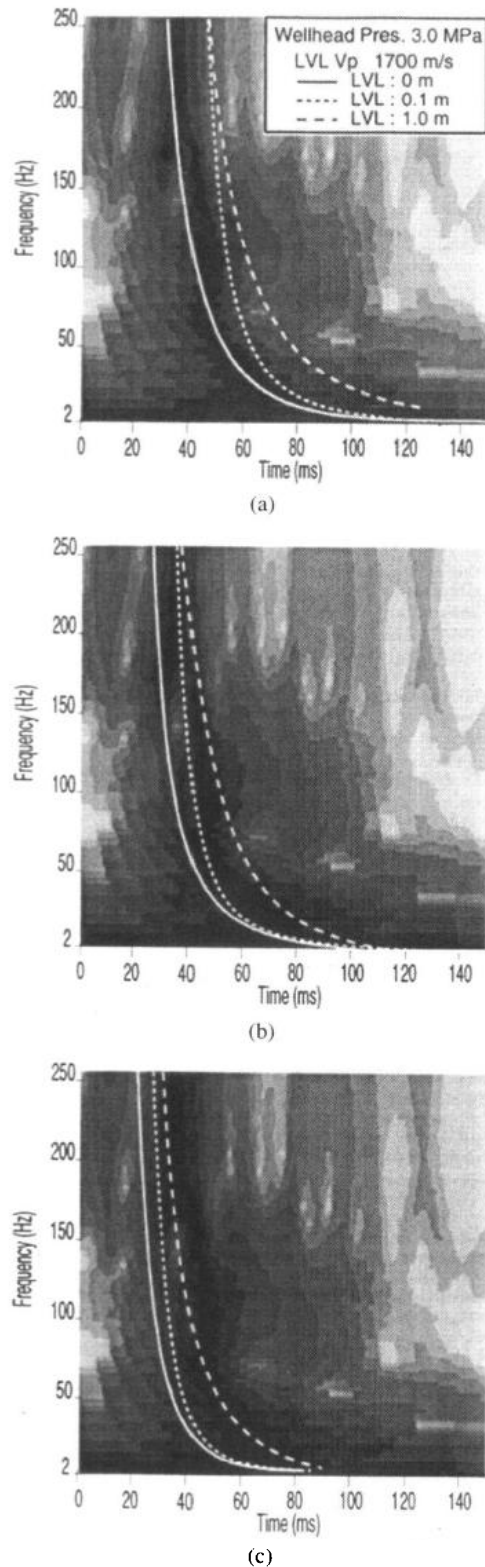


Fig. 11. Arrival times calculated with the LVL model and a time-frequency representation of crack-waves at a wellhead pressure of 3.0 MPa. (a)–(c) The fluid layer is 0.5, 1.0, and 2.0 mm thick, respectively. Compressional and shear wave velocities are 1700 and 1020 m/s, respectively. Dispersion curves are calculated at LVL thicknesses of 0, 0.1, and 1.0 m in (a) and (b).

arrival-time curves calculated with the LVL model. This wellhead pressure is higher than that in Fig. 10. A transmissibility test showed that the aperture in the artificial subsurface fracture increased at a wellhead pressure of 2.0 MPa [13]. The velocity of a compressional wave of the LVL was 1700 m/s at this wellhead pressure (Fig. 3). This velocity is lower than that at the begin-

ning of water injection. Therefore, it is reasonable to assume that the geometry of the LVL varied due to the increase in wellhead pressure.

Fig. 11 shows some arrival-time curves for crack-waves recorded at a wellhead pressure of 3.0 MPa. These crack-waves are more dispersive than those at a wellhead pressure of 0.4 MPa. Differences between the dispersions are observed at frequencies below 70 Hz. Differences between the arrival-time curves and the crack-waves measured at a wellhead pressure of 3.0 MPa are smaller than those at a wellhead pressure of 0.4 MPa. However, none of the arrival-time curves showed a good fit over the entire frequency range of 2–256 Hz. When the fluid layer is 2.0 mm and the LVL is 0.1 m, the arrival-time curve shows a good fit with the onset of the relative maxima in our trials, even though the fit is not exact.

Differences between the arrival-time curves and the measured crack-waves decreased when the wellhead pressure increased. This means that the LVL model is more suitable for a highly pressurized subsurface fracture rather than for a closed subsurface fracture. However, the estimated thicknesses of the fluid layer and the LVL are not consistent with other data (i.e., the transmissibility test and crack-wave measurement). When the fluid layer is 2.0 mm and the LVL is 0.1 m, the arrival-time curve showed a good fit to the crack-waves recorded at a wellhead pressure of 3.0 MPa in our trials. On the other hand, the thickness of the fluid layer was estimated to be 0.2 mm even at a wellhead pressure of 3.0 MPa in the transmissibility test [13]. The compressional wave velocity of rock is 3100 m/s in this field and 1700 m/s in the vicinity of the fracture at a wellhead pressure of 3.0 MPa. The air gun was suspended two meters above the intersection of a fracture, and the hydrophone was installed at another intersection. The estimated thickness (0.1 m) of the LVL is too thin to decrease compressional wave velocity in the vicinity of the fracture. If the thickness of the LVL increases, the fluid layer should be thicker than 2.0 mm in the LVL model. However, we cannot agree with a fluid layer thicker than 2.0 mm, since a fluid layer of 2.0 mm is ten times as thick as the result of the transmissibility test. Therefore, it is impossible to simulate arrival-time curves based solely on the LVL model. We should introduce mechanisms that increase the velocity of crack-waves in the LVL model.

B. Arrival-Time Curves in the Crack-Stiffness Model

Specific crack stiffness in a direction normal to the fluid layer and the thickness of the fluid layer were examined in the crack-stiffness model. The physical properties of the bedrock layers and the fluid layer are the same as in the calculations for the LVL model. Fig. 12 shows arrival-time curves on a scalogram of crack-waves recorded at a wellhead pressure of 0.4 MPa. Combinations of crack stiffness and fluid-layer thickness were found by trial and error. Arrival-time curves for a high crack stiffness show weak dispersion. They fit the relative maxima in the scalogram better than those in the LVL model. The best combination in our trials was a crack stiffness of 90 GPa/m and a fluid layer thickness of 0.2 mm.

Calculated arrival-time curves and crack-waves, recorded at a wellhead pressure of 3.0 MPa, are compared in Fig. 13. The crack-waves at a wellhead pressure of 3.0 MPa were more

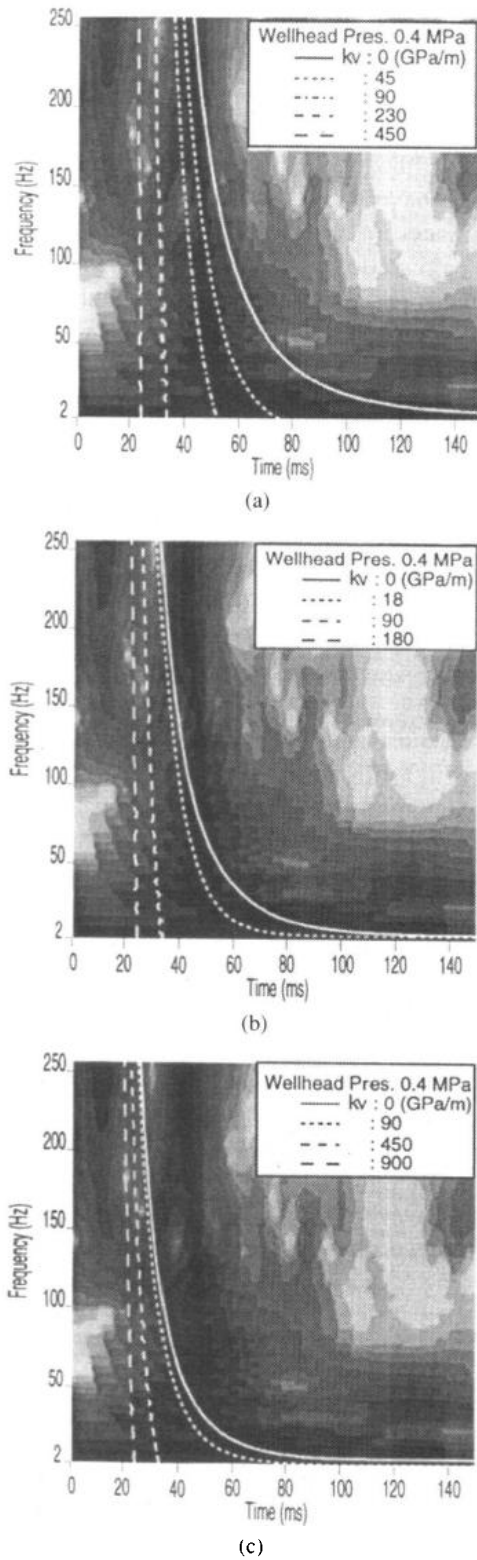


Fig. 12. Arrival times calculated with the crack-stiffness model and a time-frequency representation of the crack-waves at the beginning of water injection. (a)–(c) The fluid layer is 0.2, 0.5, and 1.0 mm thick, respectively. The arrival times of crack-waves were calculated at specific levels of crack stiffness.

strongly dispersive than those at a wellhead pressure of 0.4 MPa. When the crack stiffness is 18 GPa/m and the thickness of the fluid layer is 0.5 mm, the arrival-time curve shows a good fit to the relative maxima in the scalogram for crack-waves at a wellhead pressure of 3.0 MPa in our trials.

The estimations of crack stiffness and the thickness of the fluid layer are consistent with the opening of the fracture. When

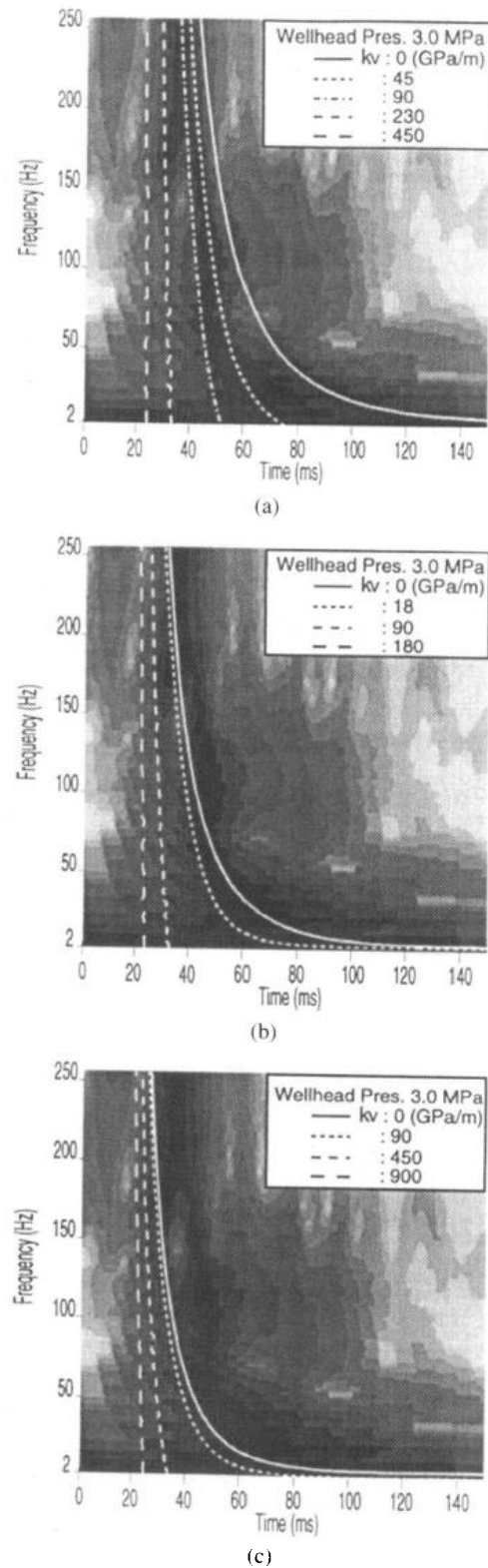


Fig. 13. Arrival times calculated with the crack-stiffness model and a time-frequency representation of crack-waves at a wellhead pressure of 3.0 MPa. (a)–(c) The fluid layer is 0.2, 0.5, and 1.0 mm thick, respectively. The arrival times of crack-waves were calculated at specific levels of crack stiffness.

the wellhead pressure increased, the thickness of the fluid layer increased from 0.2 to 0.5 mm, and the crack stiffness decreased from 90 to 18 GPa/m. In a simple model of a subsurface fracture shown in Fig. 14, stiffness per unit area in the direction normal to the interface is

$$k_v = \frac{S}{\Delta h} = \frac{E}{h} \frac{A_c}{A} \quad (9)$$

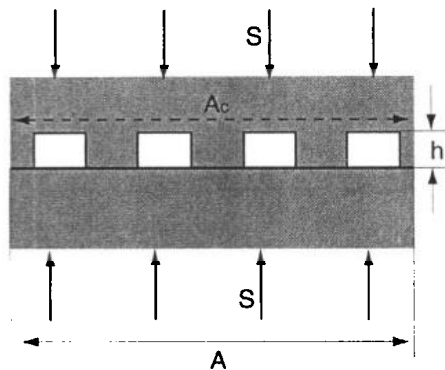


Fig. 14. Simple crack model.

where S is the compressional stress normal to the interface, A is the entire area, A_c is the contact area, and E is Young's modulus. The decrease in crack stiffness, which was observed in the crack-wave measurement, can be explained by an increase in the aperture of the fracture and by a decrease in the contact area between asperities on crack surfaces, or both.

VI. CONCLUSIONS

We have investigated the dispersions of crack-waves using two crack models. We analyzed crack-waves that were measured in an artificial subsurface fracture at a depth of about 370 m. The WT of the crack-waves measured at an artificial subsurface fracture showed positive dispersion. The crack-waves were more strongly dispersive at a wellhead pressure of 3.0 MPa than at a wellhead pressure of 0.4 MPa. The LVL model and the crack-stiffness model were used to calculate arrival-time curves of crack-waves. The arrival-time curves calculated with the LVL model were late relative to the measured crack-waves. On the other hand, the curves calculated with the crack-stiffness model agreed with the dispersions of the crack-waves. We determined the best combinations of the thickness of the fluid layer and the crack stiffness at two levels of wellhead pressure (0.4 and 3.0 MPa). These estimates with the crack-stiffness model are consistent with opening of the fracture.

We noted that contact and the low-velocity zone are important physical properties for estimating subsurface fractures. Contact is expressed in the crack-stiffness model. On the other hand, the LVL model represents a low-velocity zone. The results of the crack-wave dispersion indicate that contact is more dominant than the low-velocity zone in physical properties that affect crack-wave dispersion.

REFERENCES

- [1] B. Chouet, "Dynamics of a fluid-driven crack in three dimensions by the finite difference method," *J. Geophys. Res.*, vol. 91, pp. 13 967–13 992, Dec. 1986.
- [2] Y. G. Li, P. C. Leary, and K. Aki, "Observation and modeling of fault-zone fracture seismic anisotropy—II: P-wave polarization anomalies," *Geophys. J. R. Astron. Soc.*, vol. 91, pp. 485–492, 1987.
- [3] M. Lou, J. A. Rial, and P. E. Malin, "Modeling fault-zone guided waves of microearthquakes in a geothermal reservoir," *Geophysics*, vol. 62, pp. 1278–1284, July/Aug. 1997.
- [4] K. Nagano, H. Saito, and H. Niitsuma, "Guided waves trapped in an artificial subsurface fracture," *Geotherm. Sci. Technol.*, vol. 5, no. 1/2, pp. 63–70, 1995.

- [5] K. Nagano and H. Niitsuma, "Crack stiffness from crack wave velocities," *Geophys. Res. Lett.*, vol. 23, pp. 689–692, Mar. 1996.
- [6] K. Nagano, K. Sato, and H. Niitsuma, "Polarization of crack waves along an artificial subsurface fracture," *Geophys. Res. Lett.*, vol. 23, pp. 2017–2020, Aug. 1996.
- [7] K. Nagano, "Crack-wave dispersion at a fluid-filled fracture with low-velocity layers," *Geophys. J. Int.*, vol. 134, pp. 903–710, Sept. 1998.
- [8] K. Hayashi and K. Sato, "A theoretical study of AE traveling through a fluid-filled crack with application to characterization of a geothermal reservoir crack," in *Progress in Acoustic Emission VI*, T. Kishi, K. Takahashi, and M. Ohtsu, Eds. Tokyo, Japan: Japanese Soc. NDI, 1992, pp. 423–430.
- [9] H. Niitsuma and H. Saito, "Characterization of a subsurface artificial fracture by the triaxial shear shadow method," *Geophys. J. Int.*, vol. 107, pp. 485–491, Nov. 1991.
- [10] K. Tanaka, H. Moriya, H. Asanuma, and H. Niitsuma, "Detection of travel time delay caused by inflation of single artificial fracture," *Geotherm. Sci. Technol.*, to be published.
- [11] V. Ferrazzini and K. Aki, "Slow waves trapped in a fluid-filled infinite crack: Implication for volcanic tremor," *J. Geophys. Res.*, vol. 92, pp. 9215–9223, Aug. 1987.
- [12] H. Niitsuma, "Fracture mechanics design and development of HDR reservoirs—concept and results of the Γ -project, Tohoku University, Japan," *Int. J. Rock Mech. Min. Sci. Geomech. Abstr.*, vol. 26, no. 3/4, pp. 169–175, 1989.
- [13] K. Hayashi and H. Abé, "Evaluation of hydraulic properties of the artificial subsurface system in Higashihachimantai geothermal model field," *J. Geotherm. Res. Soc. Jpn.*, vol. 11, no. 3, pp. 203–215, 1989.
- [14] F. Hlawatsh and G. F. Boudreaux-Bartels, "Linear and quadratic time-frequency signal representations," *IEEE Signal Processing Mag.*, vol. 9, pp. 21–67, Apr. 1992.
- [15] S. Qian and D. Chen, *Joint Time-Frequency Analysis, Methods and Applications*. Englewood Cliffs, NJ: Prentice-Hall, 1996.
- [16] L. J. Pyrak-Nolte and D. D. Nolte, "Wavelet analysis of velocity dispersion of elastic interface waves propagating along a fracture," *Geophys. Res. Lett.*, vol. 22, pp. 1329–1332, June 1995.
- [17] R. Kronland, J. Morlet, and A. Grossmann, "Analysis of sound patterns through wavelet transforms," *Int. J. Pattern Recognit. Artif. Intell.*, vol. 1, no. 2, pp. 273–302, 1987.
- [18] N. A. Haskell, "The dispersion of surface waves on multilayered media," *Bull. Seismol. Soc. Amer.*, vol. 43, pp. 17–34, 1953.
- [19] K. Hayashi, T. Ito, and H. Abé, "In situ stress determination by hydraulic fracturing—A method employing an artificial notch," *Int. J. Rock Mech. Min. Sci. Geomech. Abstr.*, vol. 26, no. 3/4, pp. 197–202, 1989.

Koji Nagano received the B.Eng., M.Eng., and the Dr.Eng. degrees in electrical engineering from Tohoku University, Sendai, Japan, in 1983, 1986, and 1989, respectively.

From 1989 to 1991, he was a Fellow of the Japan Society for the Promotion of Science for Japanese Junior Scientists. He was a Research Associate at the Department of Resources Engineering, Tohoku University from 1991 to 1992, and then joined the Department of Computer Science and Systems Engineering, Muroran Institute of Technology, Muroran, Japan, where he is currently a Research Associate. His research interests are seismic signal processing, cross-hole seismic measurement, and wave propagation for characterization of subsurface crack.

Hiroaki Niitsuma received the Ph.D. degree from Tohoku University, Sendai, Japan, in 1975.

He has been a Professor with the Department of Geoscience and Technology, Faculty of Engineering, Graduate School of Tohoku University since 1988. His recent research interests are in multicomponent seismic measurement and signal processing, bore hole measurement, and characterization of geothermal reservoir. He is a Representative of the International Collaboration Program "Establishment of new mapping/imaging technologies for advanced energy extraction from deep geothermal reservoirs (MTC project)," funded by NEDO and MESC. He was Chairman of the Subsurface Instrumentation Division of MMIJ from 1989 to 1995. He is now a Director of SEGJ, MMIJ, the SPWLA Japan Chapter, and a Councilor of the Geothermal Research Society of Japan.

Area-Based Results for Mine Detection

Erol Gelenbe, *Fellow, IEEE*, and Taşak Koçak, *Member, IEEE*

Abstract—The cost and the closely related length of time spent in searching for mines or unexploded ordnance (UXO) may well be largely determined by the number of false alarms. False alarms can result in time consuming digging of soil or in additional multi-sensory tests in the minefield. In this paper, we consider two area-based methods for reducing false alarms. These are: a) the previously known “declaration” technique [8], [10] and b) the new δ technique, which we introduce. We first derive expressions and lower bounds for false-alarm probabilities as a function of declaration area and discuss their impact on receiver operation characteristic (ROC) curves. Second, we exploit characteristics of the statistical distribution of sensory energy in the immediate neighborhood of targets and of false alarms from available calibrated data, to propose the δ technique, which significantly improves discrimination between targets and false alarms. The results are abundantly illustrated with statistical data and ROC curves using electromagnetic-induction sensor data made available through DARPA [8] from measurements at various calibrated sites.

Index Terms—Area-based techniques for detection, declaration, δ technique, detection of unexploded ordnance (UXO), electromagnetic induction sensors, mine detection.

I. INTRODUCTION

AUTOMATIC mine detection and the detection of unexploded ordnance have become a subject of great importance, and a variety of sensors and processing systems have been proposed recently for mine remediation. A number of novel technical approaches to this major problem have emerged based on a variety of sensor technologies [9], [11]–[15], and the field is now on the verge of significant scientific and technical development. All approaches are based on the on-line or off-line algorithmic processing of data from single or multiple sensors and on data-fusion techniques that can take advantage of the complementary characteristics of different sensors. In this framework, availability of multisensory data [8] from calibrated minefields (and from minefields that offer significant challenge to detection algorithms) are particularly useful.

In remedial mine detection, which is primarily directed toward an exhaustive removal of mines for humanitarian purposes, both the probability of correct detection of a mine and the probability of false alarm, are important performance metrics for any sensor or processing algorithm. The probability of detection is important for obvious reasons. However, the probability of false alarm is also of major importance for simple reasons of cost. The

number of false alarms is bound to be significantly greater than the number of mines found in a given area. Hence, the cost and the closely related duration of the search for mines may well be largely determined by the large number of false alarms that will lead to unnecessary and time consuming digging of soil in the minefield. Thus, all sensors and algorithms need to address these important metrics.

There have been several studies of mine detection using statistical methods and involving different sensors, including [1]–[7], [12], [14]–[19]. In the case of the direct point-by-point exhaustive detection and search for mines, which is directly related to the present work, current detection techniques do not provide sufficiently high performance results, especially in cases where the minefield is heavily cluttered [9], [10]. Indeed, it can be expected that clutter will be prevalent in many minefield environments, since the same areas will have been used by troops in the field (littering the area with cans or spent cartridges), or simply because the minefields of interest in remedial demining may be located in populated areas. Similarly, areas that contain a lot of unexploded ordnance, such as firing ranges on or close to military bases, will contain a variety of metallic objects or other clutter which results from long term human presence. Thus, most technologies in use or that have been proposed for detecting land mine and unexploded ordnance (UXO) will typically lead to high false-alarm rates, even at relatively low probabilities of correct detection [8], [10]. Thus, the objective of this research is to develop technologies that provide accurate detection of mines in cluttered environments, with acceptably low false-alarm rates.

In order to summarize the basic concepts related to mine detection, it may be helpful to consider the summary representation of Table I. We see that if a mine exists at some location, the detector that visits that location will either correctly detect it or will miss it. On the other hand, if a mine does not exist at the location being examined, either the detector will incorrectly detect a mine yielding a false alarm, or it will correctly indicate that it does not exist.

The minefield data we will use in this study is based on measurements provided by DARPA [8], with two different electromagnetic-induction sensor systems at a variety of geographic locations. This data has been collected in a series of systematic minefield-sensing experiments, which have been conducted at multiple locations with a variety of sensors and implanted with decoy mines and mine-like objects. The first sensing system considered is a Geonics EM61-3D three-component, time-domain sensor. It consists of a multichannel pulsed-induction system, having a 1-m square transmitter coil and three orthogonal 0.5-m receiver coils, which are positioned approximately 0.3 m above the ground. The second system consists of a 0.5 m Geonics EM61 pulsed-induction sensor equipped with two

Manuscript received August 26, 1997; revised July 13, 1998. This work was supported in part by the MURI on Demining, under U.S. Army Research Office Grant DAAH04-96-1-0448.

E. Gelenbe is with the School of Electrical Engineering and Computer Science, University of Central Florida, Orlando, FL 32816 USA (erol@cs.ucf.edu).

T. Koçak is with Mitsubishi Semiconductor America, Durham, NC 27704 USA (e-mail: tkocak@ee.duke.edu).

Publisher Item Identifier S 0196-2892(00)00003-6.

TABLE I
DIFFERENT EVENTS RELATED TO MINE DETECTION

Buried Mine	Detected?	Result
EXISTS	YES	CORRECT DETECTION
EXISTS	NO	MISSED TARGET
DOES NOT EXIST	YES	FALSE ALARM
DOES NOT EXIST	NO	CORRECT NON-DETECTION

coplanar 0.5-m coils with a vertical spacing of 0.4 m. The sensor height above ground level is again approximately 0.3 m. Specifically, the data we will use represents the measurements collected in a roughly 100×100 square-meter area for four different regions. In order to be consistent with data description, we will use the following names for these regions, which will prove to have significantly different clutter characteristics, as well as different target (decoy mine) locations. They will refer to them as firing point (FP) 20, firing point (FP) 22, Seabee, and Turkey Creek. An example of EMI energy data is shown on Fig. 1 for 1-m Z-Coil measurements obtained by DARPA [8]. The vertical lines simply indicate target locations and do not represent energy values. The area that appears to have zero energy is simply an area for which we do not have any data (e.g., it may not have been surveyed). Inspection of the figure shows the significant amount of clutter in various areas and the relatively low energy levels at target locations.

The EMI energy level we use is a derived quantity from DARPA's raw data.

- 1) For 1-m data, the Geonics EM61-3D sensor data was collected along survey lines spaced 1 m apart in the east direction and at a rate of three samples per second, or at approximately 0.4-m intervals in the north direction. For each measurement point, the instrument's output is measured and recorded at 20 geometrically spaced time gates covering a time range from $320 \mu\text{s}$ to 32 ms. The energy level we use for each point is derived as follows:

$$E = \sum_{i=1}^{20} X^2(i) \quad (1)$$

where $X(i)$ is the EM61-3D sensor output for the i th time interval.

- 2) The 0.5-m data was collected along survey lines spaced at 0.5-m intervals in the east direction and 0.2-m intervals in the north direction. For this data, the received signal's absolute value from the Geonics EM61 is integrated from 0.18 to 0.87 ms after each transmit pulse, resulting in a single data point Y for each location. The energy level for each point is then simply obtained as $E = Y^2$.
- 3) Because of the relative inaccuracy of the position measurements, the minefields considered are artificially gridded on the basis of $1 \text{ m} \times 1 \text{ m}$ blocks. All the energy data is then mapped by averaging it onto this grid. Specifically, for both the 1-m and 0.5-m data, the energy values are averaged on the $1 \text{ m} \times 1 \text{ m}$ block, which contains the points where the values are measured.

As mentioned earlier, a source of inaccuracy in the practical use of the data we employ in this study is related to the exact

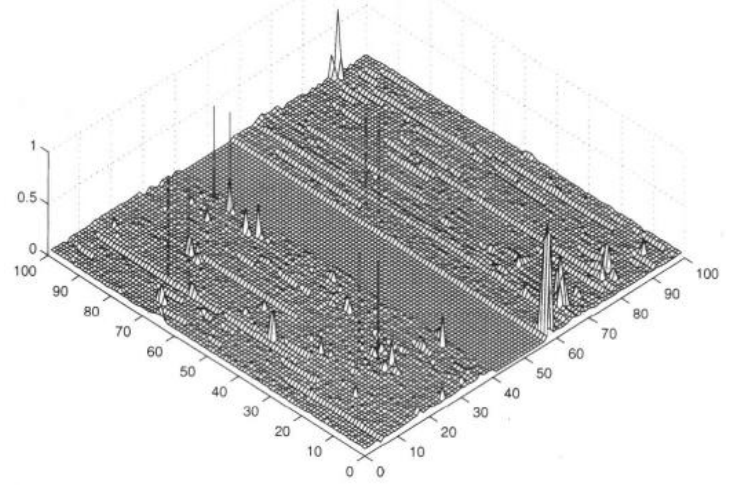


Fig. 1. Relative energy values measured at FP 20 site at 1 m resolution from the Z coil of the Geonics EM61-3D sensor. Vertical lines show some mine positions, illustrating the difficulty of detecting mines directly from measured energy.

location of the sensor being used as data was registered. This is due to a variety of instrumentation and data-collection effects, leading to errors in registering the sensor's position as it travels continuously across the minefield. Hence, we have followed a commonly accepted procedure suggested for using this data, which is to register the mine locations by analyzing the energy levels near the approximate known mine locations. We assume that if there is a mine at a particular point, then its immediate neighbors should have lower energies. To give an idea of this effect, two of the $5 \text{ m} \times 5 \text{ m}$ regions that we examine are shown in Fig. 2.

II. EFFECT OF "DECLARATION" ON FALSE ALARMS AND ROC

An established practice [8], [10] in processing minefield data is the so-called process of "declaration," which is based on the simple remark that whenever a false alarm or a mine is detected (i.e., whenever the sensor and detection algorithm says "alarm"), an area at and around the position at which the signal was detected is thoroughly searched. This search will typically involve visual inspection and perhaps digging with specialized tools and probes, but also will often entail the use of other sensors. Thus, when an alarm occurs, an area that includes that point is thoroughly checked out and all mines are found or no mines are found (i.e., it was a false alarm). It is convenient to simplify the area explored as being an $h \times h$ area centered at the point at which the detection occurred, where h is in an appropriate unit (e.g., in meters).

h is taken to be an odd integer, so that the center point of the area is the location of detection. Because of the important effect declaration has on false-alarm rates, in this section, we derive some bounds on false-alarm probabilities with declaration as compared to false-alarm probabilities obtained without declaration.

In practice, the choice of h will depend on the search procedure being followed in the field. Thus, several authors [10], [12] present ROC curves for different sensors and processing

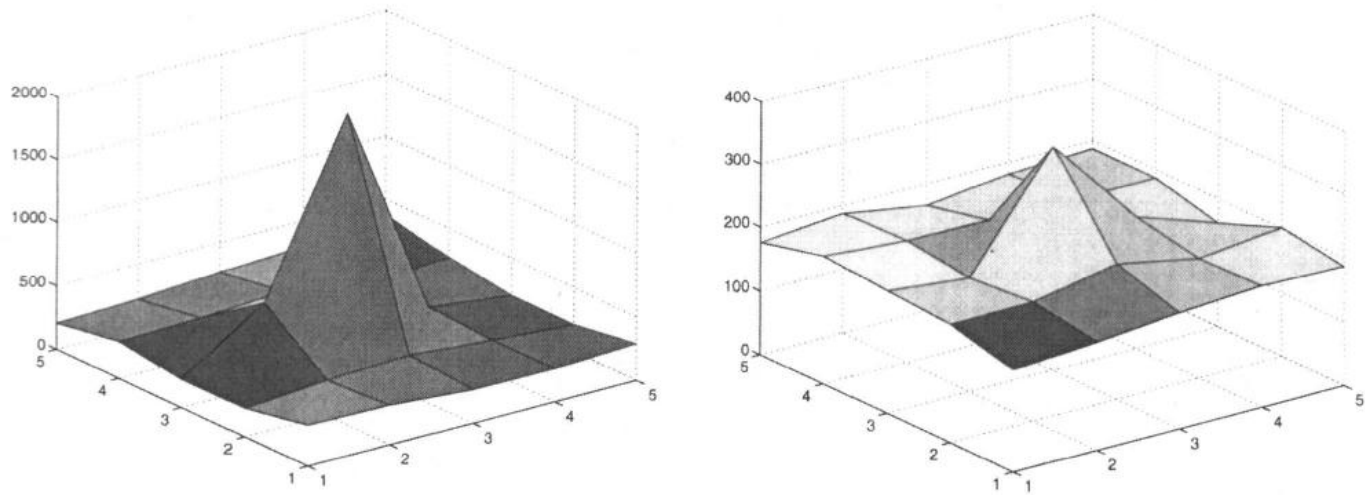


Fig. 2. Energy profiles at two mine locations in the FP 20 site (left) and the Turkey Creek site (right). The Y-axis shows the measured Z-coil energy values.

algorithms for a range of values of h varying between $h = 1$ (when the declaration procedure is simply not being used) to $h = 3, 5, 7$. Notice that a 49-m^2 area may be considered to be excessively large for a search around a presumed mine when the unit is in meters. However, when we are dealing with half-meter grids for the minefield, an approximately 12-m^2 search area corresponding to $h = 7$ might be a reasonable value to consider.

Whenever a mine or a false alarm is located at some point p , the $h \times h$ set of points $A_h(p)$ centered at p will be considered to have been explored and will be removed from further consideration concerning false-alarm rates. By "point" p , we mean some location $p = (x, y)$ in the minefield, assuming that the whole field has been discretized in 1×1 unit squares, so that point $(0, 0)$ would in fact refer to the square contained in the vertices $(0, 0), (0, 1), (1, 0), (1, 1)$. Note that if some point $q \in A_h(p)$ has been included previously in the declaration area of some other point p' where a mine or false alarm has previously been detected, then q should not be eliminated twice from the areas being scanned. In general though, it is of interest to have a theoretical understanding of how the procedure of declaration affects ROC curves. However, the precise effect of h on the ROC curves is particularly difficult to determine theoretically, since it depends on the distribution of mines and of false alarms in the field, and especially on their proximity to each other. An exact computation of the effect of h would have to make assumptions about the spatial statistics of targets and false alarms, and would therefore be poor estimates of the results obtained with real data. Therefore, in this section we derive robust bounds, which do not depend on statistical assumptions or on the nature of a particular minefield, for the impact that h will have on the probability of false alarm and the probability of correct detection.

Let us first develop some notation. Consider a minefield in which the mine locations are denoted by the set T , while the nonmine points where the detector may declare a false alarm (i.e., those points where the energy response to a sensor is nonzero) are denoted by the set N . We write $S = T \cup N$ and $|T|, |N|, |S|$ will be the sizes of the sets. Let $P_{f1}(h), P_{d1}(h)$ be the probability of false alarm and the probability of correct detection, respectively, when a declaration area of size $h \times h$ is used. For $h = 1$ (i.e., with no declaration, these will be denoted

P_f, P_d). Typically, we will have $|N| \gg |T|$ (i.e., we may have thousands of nonmine points in a minefield, with perhaps 10 or 20 mines). Ratios may be somewhat different if the targets sought are unexploded ordnance (UXO), but the $|N|$ would still be much larger than $|T|$. The following results are only valid for sensors or detectors that use point data and base their decisions concerning the presence or absence of a mine or of a false alarm at a given point p on sensor output [call it $E(p)$] at that single point p , rather than at its surroundings or in other areas. This differs from some of the algorithms that will be discussed later in this paper. Note that the following results refer to any given run of a detection algorithm on measured data on a specific minefield. Thus, the probabilities $P_{f1}(h), P_{d1}(h)$ are simply the ratio of measured numbers

$$P_{f1}(h) = \frac{F(h)}{|N|}, \quad (2)$$

$$P_{d1}(h) = \frac{D(h)}{|T|} \quad (3)$$

where $F(h)$ is the number of false alarms, and $D(h)$ is the number of correct detections counted with a declaration area of $h \times h$. All the following results concerning declaration (Propositions 1–3) assume that the false-alarm rate P_f with $h = 1$ is homogeneous for all points p in the minefield data. Our first result is

Proposition 1: Consider a detector that only uses sensor data measured at a point p to make decisions about that same point. Let $P_{f1}(h)$ be the false-alarm rate with an $h \times h$ declaration area. Then a lower bound for $P_{f1}(h)$ for any (odd-valued) h is given by

$$P_{f1}(h) \geq \frac{P_f - \frac{|T|}{|N|} P_{d1}(h)(h^2 - 1)}{1 + P_f(h^2 - 1)}. \quad (4)$$

Comment: The total number of false alarms in the detection procedure is $F(h) = P_{f1}(h) \cdot |N|$, and for $h = 1$, we write $F = P_f \cdot |N|$. $P_{f1}(h)$ can be empirically determined as the number of $1 \text{ m} \times 1 \text{ m}$ grid points where false alarms are detected in the whole minefield, divided by the total area size of the mine field,

when a declaration area of size h is used. Note that the number of false alarms with declaration cannot exceed the number of false alarms with $h = 1$. Also, the maximum possible number of false alarms in a declaration area is $(h^2 - 1)$.

Proof of Proposition 1: The expected number of false alarms in a declaration area is $P_{f1}(h)(h^2 - 1)$, while the expected number of targets detected in that area is $P_{d1}(h)(h^2 - 1)$. For each of the $|N|P_{f1}(h)$ false alarms, on the average, $P_f(h^2 - 1)$ are eliminated by the effect of the declaration, since they would have been counted as false alarms with $h = 1$. However, they are not counted with an $h \times h$ declaration area. Therefore

$$|N|P_{f1}(h) \geq P_f|N| - |N|P_{f1}(h).P_f(h^2 - 1) - |T|P_{d1}(h).P_f(h^2 - 1) \quad (5)$$

where the second term on the right-hand side is the average number of false alarms that are eliminated from the false alarms with declaration, while the third term is the average number of false alarms that are eliminated by the targets detected with declaration. Dividing all terms in (5) by $|N|$, we remain with

$$P_{f1}(h) \geq P_f - P_f.P_{f1}(h)(h^2 - 1) - P_{d1}(h).P_f(h^2 - 1) \frac{|T|}{|N|}, \quad (6)$$

or

$$P_{f1}(h) \geq \frac{P_f \left[1 - P_{d1}(h).(h^2 - 1) \frac{|T|}{|N|} \right]}{1 + P_f(h^2 - 1)}. \quad (7)$$

Q.E.D.

Because $|N| \gg |T|$, the simpler approximate inequality

$$P_{f1}(h) \geq \frac{P_f}{1 + P_f.(h^2 - 1)} \quad (8)$$

can be used, which has the added advantage of not requiring knowledge of $P_{d1}(h)$.

In Fig. 3, we compare the lower bound provided by (8) with empirical false alarm probabilities obtained with various values of h for a specific set of data from [8] on the FP 20 Site. We observe that the resulting ROC curves which use the lower bounds of $P_{f1}(h)$ are, as one would expect, optimistic with respect to real data. An upper bound to the false alarm probabilities with declaration would also be quite useful.

Notice that if the false-alarm probability in the vicinity of a false alarm that has been discovered is different from P_f like a value \hat{P}_f that may occur when false alarms are highly correlated spatially, then the lower-bound formula (8) becomes

$$P_{f1}(h) \geq \frac{P_f}{1 + \hat{P}_f.(h^2 - 1)}. \quad (9)$$

III. AN AREA-BASED DETECTOR: THE δ TECHNIQUE

False alarms are the major source of needless time expenditure in the search for mines. Thus, significant reductions of false-alarm rates are very valuable. In this section, we will propose and evaluate a method that significantly reduces

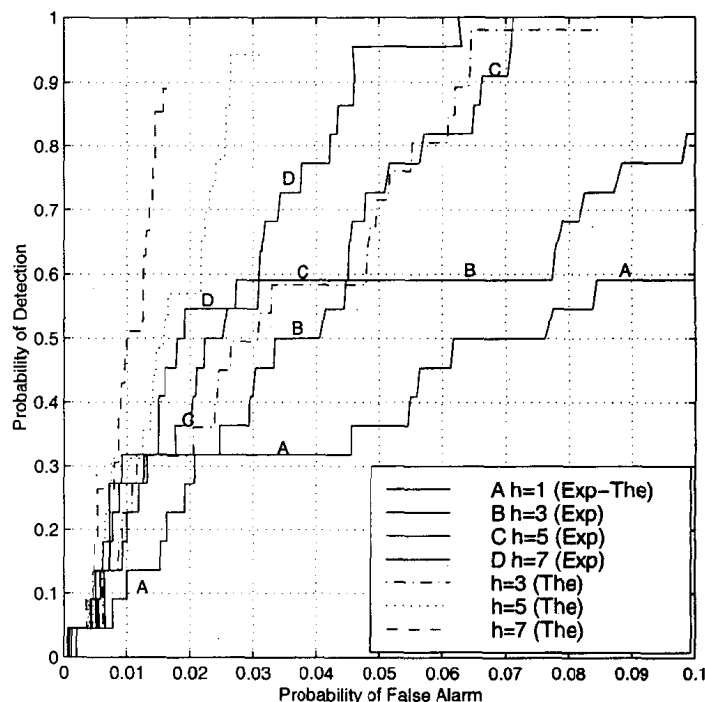


Fig. 3. Effect of declaration.

false-alarm rates by making use of neighborhood or area information around each point visited during the search.

Consider again the energy measurements around two mine locations shown in Fig. 2, where we see that the energy at the mine location is higher than that at neighboring points. If this is generally true of most mine locations, and if this property were much less frequent in nontarget areas, we would hold a very good lead into a manner of reducing false alarms. In order to see whether such an idea can be fruitfully pursued, we examine the following statistic of the Z-coil data from all of the measured sites with the electromagnetic induction (EMI) sensors

$$D_n(p) = \frac{E(p) - E(p_n)}{E(p)} \quad (10)$$

where p is any point in the minefield, $E(p)$ is the EMI energy level measured by the Z-coil at point p , and $E(p_n)$ is the energy level of an immediate neighbor (there are eight of them) of the point p . $D_n(p)$ in (10) is relative to the center-point energy $E(p)$, so as to generate relative rather than absolute values. We call D_n the "local relative energ." Notice that $D_n(p) \leq 1$, but that it can take unbounded negative values. We note that $D_n(p)$ is a quantity related to some specific neighbor n of point p , so that no averaging over the eight neighbors of p is implied in (10). The local relative energy is a derived statistic we introduce, while the energy measurements themselves are available in the data from the DARPA clutter experiment. Note that each point p gives rise to eight distinct values that appear in these histograms.

Measured histograms of $D_n(p)$ for all p that are mine and nonmine locations for all available data are shown in Figs. 4–7. Also, these histograms all relate to the same set of mines that are artificially planted in them in the same relative positions and at approximately the same depth. Thus, the differences in the energy statistics of different sites are a result of the clutter and soil

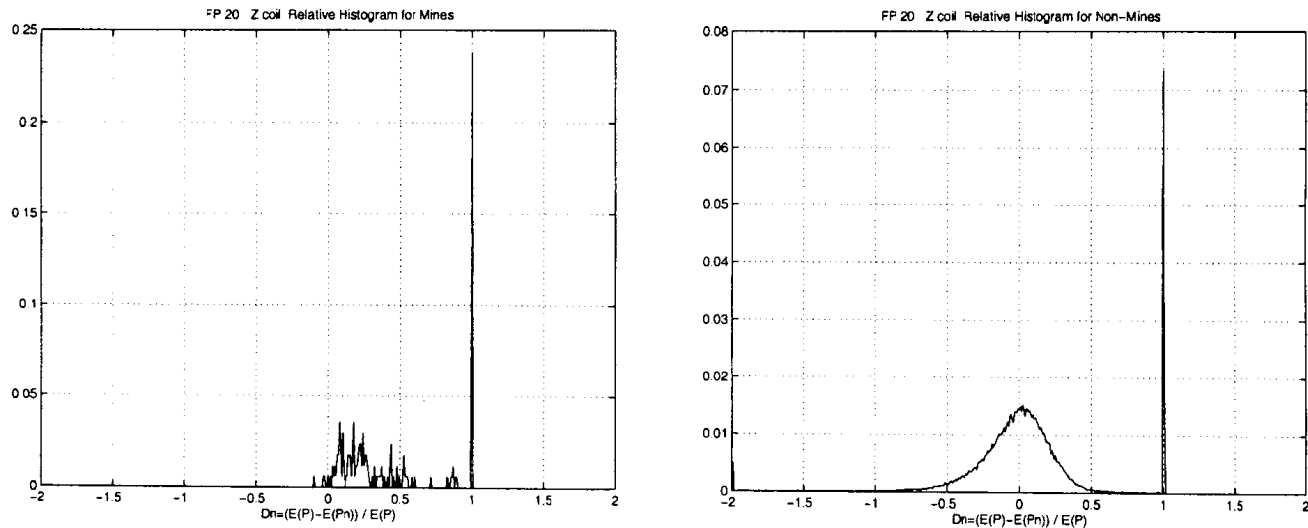


Fig. 4. Relative histogram (y -axis is the probability) of local relative energy of all mine (left) and nonmine (right) locations for FP 20.

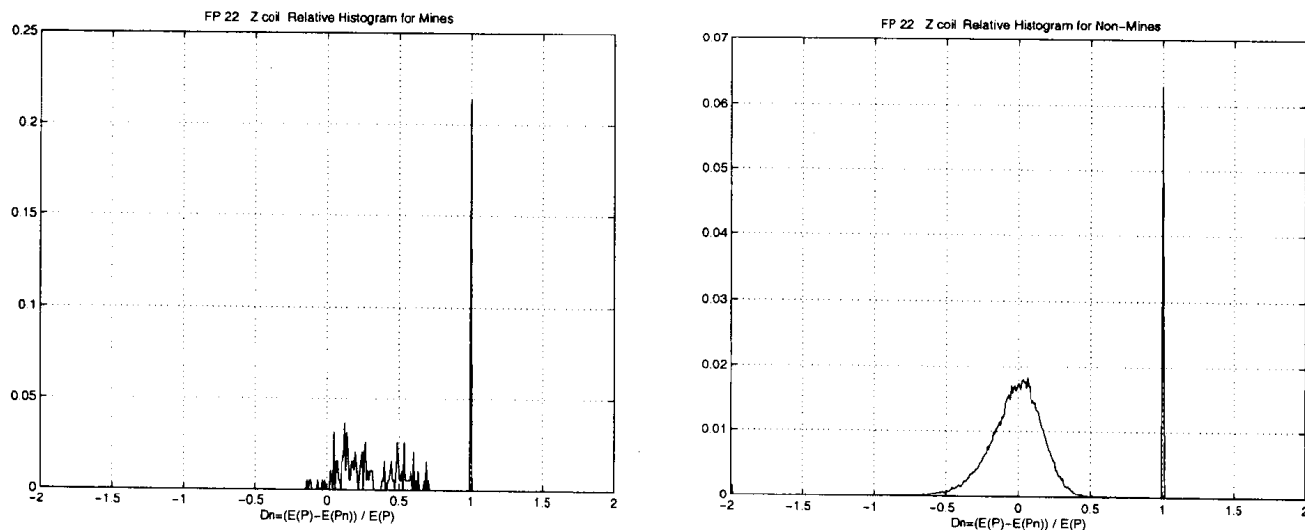


Fig. 5. Relative histogram (y -axis is the probability) of local relative energy of all mine (left) and nonmine (right) locations for FP 22.

characteristics. The clutter is a result of naturally occurring effects, as well as of various objects that may be present in the minefield without anyone's explicit knowledge. For instance, each of these areas has been actively used in the past as firing ranges, training areas, etc. Therefore, the areas will contain debris from previous usage, which will contribute in some random fashion to the clutter.

From these histograms, we always notice an accumulation point close to the value $D_n(p) = 1$, which corresponds to the case in which the neighboring points to point p exhibit very small relative energy. Other than that, we notice a very marked difference between histograms at mine locations compared to histograms at other points. At mine locations, most of the neighboring energy values are smaller than at p , so that $D_n(p)$ is positive most of the time. However, at nonmine locations, the distribution of energies is quasi-equal on either side of the energy value at p .

These observations provide us with a simple but very useful improvement on the energy detector, which we shall call the δ technique, where δ is used to denote "difference,"

- 1) For any selected threshold energy level θ , select all data points p where the Z-coil EMI energy $E(p) \geq \theta$. Call this set $H(\theta)$.

- 2) Select a number $m = 1, \dots, 8$. For each p in $H(\theta)$, count the number of immediate neighbors P_n whose energy value is strictly less than $E(p)$, and call it $M(p)$. Notice that $M(p) \leq 8$. If $M(p) \geq m$, classify p as a mine. Otherwise, treat it as a nonmine. Clearly, many p 's thus classified as mines will turn out to be false alarms.
- 3) We will say that $\delta = m/8$ (and in practice for many of our numerical examples we have selected $\delta = 7/8$ or $8/8$), because of the very significant clutter-rejection capabilities of these parameter settings, as shown in Fig. 8.

The effect of the δ technique on false alarms is illustrated in Fig. 8 as a function of the energy threshold θ of the detector. As the actual value of δ increases, the percentage of false alarms rejected will vary from a low value of 10% to a high value of 85%. Thus, the δ technique will significantly impact the ROC curves of an energy detector by reducing the false-alarm rates. Fig. 9 shows the ratio of false-alarm probabilities $P_f^{\delta}(h)/P_{f1}(h)$ for the two extreme cases $h = 1$ (no declaration) and $h = 7$ at the FP 20 Site, as a function of the energy threshold θ . The significant reduction in false-alarm probabilities is present even with a very large declaration area. We observe the same effect on all the other sites but